UNRAVELLING METAL BINDING ON MODIFIED BAUXITE REFINERY RESIDUES

Clark MW [a*], Payne TE[b], Collins RN[b,c], Harrison JJ[b], Johnston M[a] and Comarmond MJ[b]

[a.] *School of Environmental Science and Management, Southern Cross University, PO Box 157, Lismore, NSW 2480, Australia*

[b.] *Institute for Environmental Research, ANSTO, Locked Bag 2001, Kirrawee, NSW 2232, Australia.*

[c.] *School of Civil and Environmental Engineering, University of New South Wales, Sydney NSW 2052, Australia.*

Abstract

Seawater neutralised modified bauxite refinery residues (MBRR), such as Bauxsol™, are used in environmental remediation, especially in the treatment of acidic, trace-metal-rich fluids, however, there is very little knowledge on how metals are retained by MBRR. The binding for Cu, Cr, Co, Mn and Zn to Bauxsol™, determined by X-ray absorption spectroscopy (XAS); and reversibility of U(VI) and Th, studied by isotopic exchange, are presented in this paper. XAS data indicate that metal uptake primarily occurred through precipitation reactions, and that sodalite, gibbsite and hematite are the three key minerals involved in the immobilisation within Bauxsol™. Cu uptake was a function of both sorption (dimeric surface complexes) and surface precipitation ($Cu(OH)_2$) reactions on hematite. Cr(III) immobilisation occurred on hematite and sodalite as multinuclear sorption complexes and/or precipitation as γ-CrOOH on mineral surfaces. Zn and Co are immobilised primarily through surface precipitation of hydrotalcite- and amorphous hydroxide-like solids on sodalite and/or gibbsite surfaces. Mn(II) was observed in association with hematite and sodalite, where partial oxidation to Mn(IV) plays a role in Mn immobilisation. Furthermore, U(VI) and Th isotopic exchange data shows that Th is almost entirely bound by MBRR surfaces, whereas U(VI) has pH-dependent sorption with a much larger degree of reversibility. Initial sorption data indicates a competition between U and Th for binding sites, and that about 20% of U is irreversibly bound. However, aging of the bound materials results in increased irreversibility, where intra-particle diffusion to deep mineral lattice defects is a primary mechanism of incorporation.

1. Introduction

Red muds are an ever-growing waste material, with current estimates of 120 Mt/annum and a global inventory of some 1.2 Gt [1]. There are some attempts to mitigate the legacy that red mud poses through its use as a product in environmental remediation. This is particularly true for seawater- and gypsum neutralised materials (Alkaloam™[2]) because the neutralisation processes precipitate alkalinity[3]. The precipitation of alkalinity provides the red mud with acid neutralising capacity (ANC), lowers the pH from unacceptably high pH (typically 13.5) to more environmentally benign value of 8.5 -10 (depending on how complete the neutralisation is, and how much precipitate reversion occurs post treatment [4, 5]).

Bauxite refinery residues (BRR's) and modified-BRR's (MBRR's) have a complex mineralogy, which is generated from the primary parent material mineralogy, weathering products during bauxite formation, digestion and desilication product (DSP) formation within the refinery, and neo-formed minerals during red mud neutralisation and treatment[6]. Typically a seawater-neutralised red mud contains 7 main minerals, but may include up to 30 different mineral phases (Table 1). This wide range of mineral phases and fine-grained nature should favour trace metal binding. In fact, trace metal removal by BRR and MBRRs, is well known and has been reported widely. The trace metal binding capacities of BRR, and MBRRs have been suggested to be in excess of 1,500 meq/kg [6], but is particularly difficult to determine how metals are bound to mineral surfaces and which minerals are involved. Few studies have investigated the nature of the trace metal binding environment, which minerals are involved in the binding (preferential), and how binding may change over time.

This paper presents recent data from synchrotron and isotopic exchange experiments that start un-ravelling some of the metal binding phenomena observed when seawater-neutralised materials (Bauxsol™) interact with metal cations. It presents preliminary findings on which minerals are active in the metal binding, the binding environments, how reversible the removal process is and how aging affects reversibility.

Table 1: Mineral composition of MBRR derived from Euralumina bauxite refinery residues, and modified using a Ca- and MgCl2 brine.; washing the MBRR removes soluble salts and reduces electrical conductivity.

Mineral	Unwashed			Washed		
	Min	Max	Mean	Min	Max	Mean
Iron (hydr)oxides[1]	30	35	31.6	30	35	33.3
Aluminium (hydr)oxides[2]	15	20	17.9	15	20	18.1
Sodalite	15	20	17.3	15	8	17.8
Quartz (SiO_2)	5	8	6.8	5	8	7.0
Cancrinite	5	8	6.5	5	6	6.5
TiO_2 (anatase & minor rutile)[3]	4	6	4.9	4	6	5.0
Ca(Al)hydroxides & hydroxycarbonates[4]	4	6	4.5	4	6	4.6
Mg(Al)hydroxides & hydroxycarbonates[5]	3	5	3.8	3	5	3.9
Ca carbonates[6]	2	4	2.3	2	4	2.2
Halite	2	3	2.7	0	0.1	0.03
Others[7]	1	2	1.7	1	2	1.7

[1] includes dominant hematite, but also ferrihydrite, goethite, magnetite and lepidocrocite; [2] includes dominant gibbsite, but also boehmite, bayerite, and diaspore; [3] although concentration for Euralumina derived Bauxsol™ is low other residues contain up to 15% TiO_2; [4] includes: hydrocalumite and p-aluminohydrocalcite, and portlandite; [5] includes: dominant hydrotalcite and brucite, [6] includes: calcite and aragonite; [7] includes: chromite, monazite, zircon, fluorite, euxinite, gypsum, anhydrite, bassinite, whewellite, and weddelite

2. Methods

2.1 Mineral Phases

The MBRR for this work was derived from the Euralumina BRR (Sardinia), and supplied by Virotec Global solutions Pty. Ltd. The hematite standard was manufactured by the method of Schwertmann et al 1985; [7], whereas the sodalite was manufactured by taking stoichiometric proportions of gibbsite (Al(OH)3 Ajax Fine Chemicals), hydrophilic fumed silica (SiO2; Whacker Chemicals), and sodium chloride (NaCl; Ajax Fine Chemicals), and a slight excess of sodium hydroxide, which were then exposed to hydrothermal conditions in a Teflon pressure vessel at 160°C for 192hrs [8]. The Anatase was supplied by Degussa under the trade name AEROXIDE® TiO2, P 25, the gibbsite by Ajax Fine Chemicals as a Al(OH)3. XRD analysis (data not shown) of the materials indicate that the minerals synthesis provided a >93% purity hematite with minor residual ferrihydrite, >97% purity sodalite with trace SiO2, >98% pure gibbsite, and also indicate that the supplied TiO2 was 86% anatase and 14% rutile, which are in similar to proportions found in the Euralumina BRR.

2.2 XAFS and XANES analysis

A 1.25 g sample of MBRR, and standard minerals (Anatase, Hematite, Sodalite and Gibbsite) were equilibrated with 50 mL of a 10 mM solution each of 5 transition metals (Cu, Co, Cr, Mn & Zn as nitrates) and the solids gently suspended. Equilibration was made over a 196 hr period and after equilibration the samples were centrifuged, residual solids re-suspended and washed with Milli-Q water.

Measurements around the Cr, Mn, Co, Cu and Zn K-edge of samples were undertaken on the Australian National Beamline Facility at the Photon Factory (KEK Tsukuba, Japan); a 2.5 GeV, 430 mA continuous injection facility. The incident X-ray beam was selected using a channel cut Si(111) monochromator, detuned by ~50% and the beam size on the sample was approximately 1 x 4 mm. Samples were held at ~ 12 K in a He-cryostat to minimise thermal disorder. Energy calibration and multiple scan merging was carried out with the software program Average[9]. Data processing was performed with the Athena software[10], where, pre-edge background subtraction and normalisation was accomplished by fitting a linear polynomial to the pre-edge region and a quadratic polynomial to the post-edge region.

The chemical forms of the metals associated with Bauxsol™ were initially assessed by linear combination fitting (LCF) of the 1st derivative XANES data as well as the k3-weighted chi(k) EXAFS spectra between 3 – 12 Å-1 with the reference mineral spectra. The ARTEMIS program was then used to generate ab initio phase and amplitude functions for determining coordination parameters of the first and second shells surrounding the metals[10]. Coordination-shell fits of RDF data were carried out in R space between 1 – 2.2 Å, and the presence of backscatters in the second coordination shell were statistically tested with the F-test[11] to give second coordination shell 1 – 3.4 Å, that was statistically improved ($p < 0.05$) over the single shell contribution.

2.3 Isotopic exchange analysis

MBRR was loaded with ^{232}Th or ^{238}U and equilibrated over 8 days (192 hrs) with a solid to liquid ratio of 1 g of MBRR per 40 mL of 0.4 mM and 0.2 mM, as ^{232}Th or ^{238}U. A mixed system containing both 0.2 mM of U and 0.2 mM of Th was also prepared. Following equilibration, sub-samples were centrifuged, and the supernatant liquor collected for analysis. MBRR solids were then placed in aqueous solutions containing ^{232}U or ^{229}Th to compare the sorption behaviour of the added uranium and thorium with the ^{238}U and ^{232}Th previously sorbed; any differences in behaviour can be ascribed to irreversible incorporation during the initial 8 day equilibration. The MBRR solids had a sequential stepwise (stat) titration from pH of 8 to pH 3, where the pH was held at a constant pH for 1 hr, before a 2 mL sub-sample collected and a rapid lowering of pH. Hence, the plot of pH against time appears as a series of flat steps; sub-samples were centrifuged through a 0.2 µm filter at 4500 rpm for 10 minutes.

The solid and liquid weights, and the volume of acid added to adjust and maintain pH at each step was tracked for mass balance of thorium and uranium isotope calculations, and determination of partitioning co-efficients (K_d). Following the pH 3.0 sampling, samples were left over night (16 hrs), and a second sampling at pH 3 made. ^{232}Th and ^{238}U concentrations and elements (e.g., Ca, Mg, & Fe) leached from the solids were determined by ICP-MS. Samples containing U and Th were also purified and separated using a radiochemical separation[12] and ^{229}Th, ^{232}Th, ^{238}U and ^{232}U radionuclides concentrations measured by alpha spectrometry; additional samples were aged for 6-months at 4, 23, and 60°C to show how aging affects binding strength.

3. Results and Discussion

3.1 Cu uptake

The normalised Cu K-edge XANES spectra, and 1st derivative data, for Cu are shown in, respectively, Figures 1a and 1f. In

these figures the similarity of the chemical form of Cu associated with the Bauxsol™ sample and hematite and anatase reference minerals are apparent. Relative to the other spectra, there is a clear shift downwards in edge energy for the spectrum of Cu associated with sodalite (Fig. 1f) indicating that the chemical form of Cu in this reference was not present in Cu- Bauxsol™. Linear combination fitting of the Cu-Bauxsol™ first derivative XANES spectrum with the Cu-hematite and -anatase spectra resulted in a best fit of 100 % Cu-hematite with an R-factor of 1.0 % (Fig. 1f), suggesting that the chemical form of Cu associated with hematite is most similar to that in the Bauxsol™ sample. It is also evident from visual examination of the EXAFS spectra (data not shown) that the coordination environment of Cu in the Bauxsol™ was most similar to that of Cu in either Cu-hematite or Cu-anatase. Indeed, results from LCF of the Cu-Bauxsol™ EXAFS spectrum indicated that the data were best fit with 72 % Cu-hematite and 28 % Cu-anatase (R-factor 12.9 %, data not shown).

To examine the structural environment of Cu in the Bauxsol™, hematite and anatase references, the EXAFS spectra were modelled based on results reported by Peacock and Sherman [13] and Cheah et al. [14]. First shell equatorial and axial O atoms could be modelled to all three spectra (Table 2). For Cu-hematite, the best fit of the data was obtained when Cu was modelled as a $Cu(OH)_2$ precipitate (Table 2 and Figures 3a and 4), despite some differences to the reported average bond lengths of the 2nd shell Cu atoms [14], which are superior to the results when data were modelled based on Cu sorbed to hematite [13]. The Cu-anatase spectrum could be reasonably modelled [14] with 2nd shell Cu and Ti atoms suggesting sorption of a dimer (Table 2). Modelling of the Cu-Bauxsol™ sample show a coordination environment of Cu with hydroxide-like components (e.g. O_{ax} atoms at 2.33 Å and 2nd shell Cu atoms at 3.00 Å and Cu/Fe atoms ~3.25 Å) but significant differences to the Cu-hematite reference were apparent e.g., when second shell Fe back-scatterers were included at 3.22 and 3.45 Å (Table 2)[13] for dimeric Cu sorbed to hematite. Consequently, Cu appears to be removed both by sorption and surface precipitation of Cu, as $Cu(OH)_2$, by Bauxsol™ onto the hematite fraction.

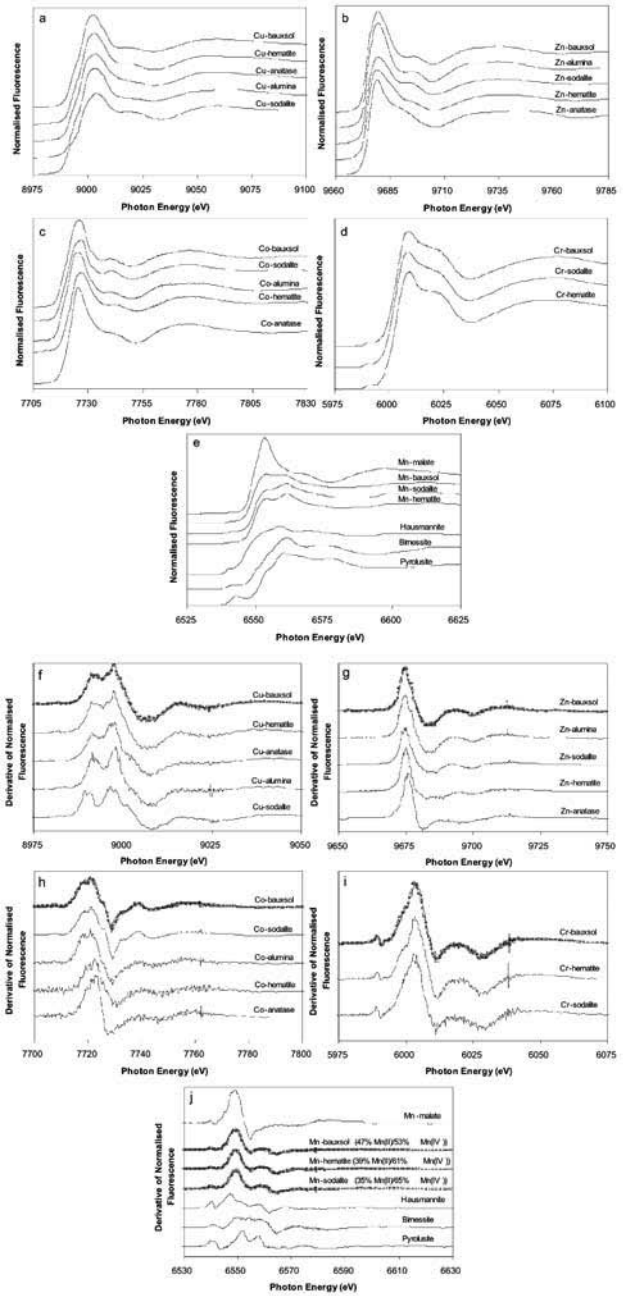

Figure 1 Normalised XANES spectra (a-e) and 1st derivative XANES spectra (f-j) of the Bauxsol™ and reference minerals. The open circles (f-j) represent the linear combination fits using the reference minerals. In the case of Mn, the spectra were fitted with Mn-malate (as Mn(II)) and birnessite (as Mn(IV)).

Table 2: Structural parameters of the metals in the Bauxsol™ and selected reference minerals based on analysis of the EXAFS data (single-scattering pathways only).

Bond	CN	R (Å)	s2 (Å^2)	DE (eV)	R-factor
Cu- Bauxsol™,, k-range 2 - 12 Å^{-1}, fitting range 1.05- 3.5 Å, S_o^2 = 0.72					
Cu-O_{eq}	3.9(0.3)	1.96 ± 0.01	0.0033 ± 0.0011	-2.5	0.016
Cu-O_{ax}	0.7(0.3)	2.33 ± 0.03			
Cu-Cu	1(0.3)	3.00 ± 0.02	0.0056 ± 0.0021		
Cu-Fe	1.5(0.4)	3.22 ± 0.01	0.058 ± 0.0030		
Cu-Fe	1(0.3)	3.45 ± 0.03			
Cu-hematite, k-range 2 - 13.5 Å^{-1}, fitting range 1.05 - 3.5 Å					
Cu-O_{eq}	4.1(0.1)	1.94 ± 0.01	0.0033 ± 0.0011	-4.2	0.011
Cu-O_{ax}	0.6(0.2)	2.38 ± 0.06			
Cu-Cu	2.2(0.8)	3.00 ± 0.01	0.0077 ± 0.0020		
Cu-Cu	4.4(0.5)	3.26 ± 0.01	0.015 ± 0.001		
Cu-anatase, k-range 2 - 13.5 Å^{-1}, fitting range 1.1 - 3.0 Å					
Cu-O_{eq}	4.1(0.3)	1.93 ± 0.01	0.0050 ± 0.0007	-7.5	0.007
Cu-O_{ax}	1.4(0.4)	2.47 ± 0.02			
Cu-Ti	1.1(0.3)	2.96 ± 0.03	0.018 ± 0.007		
Cu-Cu	1.0(0.1)	3.01 ± 0.01	0.0061 ± 0.0008		
Zn-Bauxsol™, k-range 2 - 12 Å^{-1}, fitting range 1.05- 3.3 Å, S_o^2 = 0.81					
Zn-O	5.3(0.4)	2.02 ± 0.01	0.0091 ± 0.0011	0.1	0.007
Zn-Al	0.8(0.2)	3.07 ± 0.04	0.0066 ± 0.0015		
Zn-Zn	1.6(0.1)	3.07 ± 0.01			
Zn-alumina, k-range 2 - 12 Å^{-1}, fitting range 1.1- 3.6 Å					
Zn-O	6.0(0.4)	2.03 ± 0.01	0.011 ± 0.003	-0.2	0.035
Zn-Al	1.2(0.5)	3.07 ± 0.02			
Zn-Zn	3.2(0.3)	3.11 ± 0.01	0.008 ± 0.002		
Zn-Zn	1.4(0.3)	3.57 ± 0.02			
Zn-sodalite, k-range 2 - 12 Å^{-1}, fitting range 1.1- 3.6 Å					
Zn-O	4.0(0.2)	1.96 ± 0.01	0.0067 ± 0.0005	-1.3	0.016
Zn-Zn	0.6(0.2)	3.11 ± 0.01	0.0043 ± 0.0024		
Zn-Zn	0.6(0.2)	3.55 ± 0.01			
Co- Bauxsol™, k-range 2 - 12.5 Å^{-1}, fitting range 1.0- 3.4 Å, S_o^2 = 0.83					
Co-O	5.9(0.2)	2.06 ± 0.01	0.0055 ± 0.0009	-4.6	0.011
Co-Co	4.1(0.4)	3.08 ± 0.02	0.0060 ± 0.001		
Co-Al	1.5(0.3)	3.13 ± 0.02			
Co-sodalite, k-range 2 - 12.5 Å^{-1}, fitting range 1.0- 3.4 Å					
Co-O	5.9(0.7)	2.07 ± 0.01	0.0077 ± 0.0012	-3.85	0.053
Co-Co	5.5(0.4)	3.10 ± 0.01	0.0057 ± 0.0005		
Co-alumina, k-range 2 - 12.5 Å^{-1}, fitting range 1.1- 3.4 Å					
Co-O	4.9(0.5)	2.06 ± 0.01	0.0038 ± 0.0004	-3.8	0.023
Co-Co	3(0.2)	3.09 ± 0.02	0.0067 ± 0.0025		
Co-Al	2.7(0.4)	3.11 ± 0.01			
Cr- Bauxsol™, k-range 2 - 11.5 Å^{-1}, fitting range 1.0- 3.0 Å, S_o^2 = 0.83					
Cr-O	5.6(0.5)	1.98 ± 0.01	0.0009 ± 0.0004	-2.3	0.024
Cr-Cr	1.2(0.3)	3.01 ± 0.02	0.0041 ± 0.0012		
Cr-hematite, k-range 2 - 11.5 Å^{-1}, fitting range 1.0- 3.0 Å					
Cr-O	5.9(0.5)	1.98 ± 0.01	0.0012 ± 0.0005	-2.7	0.021
Cr-Cr	1.8(0.3)	3.03 ± 0.01	0.0041 ± 0.0012		
Cr-sodalite, k-range 2 - 11.5 Å^{-1}, fitting range 1.0- 3.0 Å					
Cr-O	5.6(0.5)	1.99 ± 0.01	0.0007 ± 0.0005	-3	0.026
Cr-Cr	1.2(0.3)	3.01 ± 0.01	0.0025 ± 0.0011		
Mn- Bauxsol™, k-range 2 - 11 Å^{-1}, fitting range 1.0- 2.4 Å, S_o^2 = 0.75					
Mn-O	2.3(0.4)	1.90 ± 0.01	0.006	-3.6	0.03
Mn-O	3.2(0.4)	2.17 ± 0.02			
Mn-hematite, k-range 2 - 11 Å^{-1}, fitting range 1.0- 2.4 Å					
Mn-O	2.7(0.4)	1.90 ± 0.01	0.006	-5	0.026
Mn-O	3.2(0.2)	2.19 ± 0.02			
Mn-sodalite, k-range 2 - 11 Å^{-1}, fitting range 1.0- 2.4 Å					
Mn-O	3.5(0.5)	1.89 ± 0.02	0.006	-5.3	0.046
Mn-O	3.3(0.6)	2.18 ± 0.02			

™ Zn uptake

The normalised Zn K-edge XANES spectra and 1st derivative data of Zn associated with Bauxsol™ and the reference minerals are shown in Figures 1b and 1g and the similarities between Zn-Bauxsol™ and the Zn-alumina and -sodalite references are noteworthy; differences for Zn-anatase include a shift higher in edge energy. Linear combination fitting of the Zn-Bauxsol™ 1st derivative XANES spectrum resulted in a best fit of 71 % Zn-alumina and 29 % Zn-sodalite with an R-factor of 0.9 % (Fig. 1g). In slight contrast, linear combination fitting of the Bauxsol™ EXAFS spectrum resulted in a best fit (R-factor = 15 %) with an increased contribution (45 %) from Zn-sodalite (data not shown).

Zn uptake by aluminium (hydr)oxides has previously been examined [15, 16] where high sorption densities result in the formation of mixed-metal Zn-Al precipitates with a hydrotalcite-type local structures. Shell fitting results (Table 2) of Zn-alumina and Zn-Bauxsol™ are consistent with these other studies [15, 16]. Evidence for the existence of $Zn(OH)_2$ was also found in Zn-alumina samples [17]. However, the 1st shell O atoms were reduced in number and bond distance for the Zn-sodalite suggesting Zn primarily existed in a tetrahedral coordination environment, similar to that reported on amorphous silica at high pH values and sorption densities [16]. Given that the coordination number of 1st shell Zn-O bonds in Zn-Bauxsol™ was determined at 5.3 Å it is, likely that Zn uptake in this material was primarily facilitated through Zn-Al hydrotalcite precipitation on alumina as well as the sorption/precipitation of tetrahedral Zn on sodalite surfaces.

3.2 Co uptake

The normalised Co K-edge XANES spectra and 1st derivative data of Co associated with Bauxsol™ and the reference minerals are shown in Figures 1c and 1h. The visual similarity between Co-Bauxsol™ with the Co-sodalite and -alumina samples was confirmed with linear combination fitting of the 1st derivative XANES spectra (69 % Co-sodalite and 31 % Co-alumina, R-factor = 2.2 %; Fig. 1h). Similar results were obtained with LCF of the EXAFS data (3 - 10 $Å^{-1}$) with 58 % Co-sodalite and 42 % Co-alumina (R-factor = 12.6%) providing the best fit of Co-Bauxsol™ (data not shown).

Cobalt is also known to form hydrotalcite-like precipitates when sorbed/precipitated onto aluminium oxides and aluminosilicates [18] and the modelling of the Co-Bauxsol™`, and -alumina samples (Table 2) bond distances and coordination numbers are`, indeed`, similar to Co-Al hydrotalcite-like surface precipitates [18]. The coordination number of the 2nd shell Co-Co bonds in Co-sodalite is close to that expected for $Co(OH)_2$, hence Co uptake by sodalite appears to be more closely related to the precipitation of amorphous $Co(OH)_2$. Moreover, the coordination parameters for the local structure of Co suggest that Co uptake to Bauxsol™ is mixture of $Co(OH)_2$ and Co-Al hydrotalcite precipitates[18].

3.3 Cr uptake

Interestingly, only the hematite and sodalite reference minerals accumulated Cr(III) to concentrations comparable to that obtained when aqueous Cr(III) was reacted with Bauxsol™; Cr XAS data were collected on these two references. Figure 1d, shows that the XANES data for these three samples were all very similar. Fitting of the Bauxsol™ 1st derivative data resulted in the best fit being obtained with 65 % Cr-hematite and 35 % Cr-sodalite (R-factor = 1.6 %; Fig. 1i). Linear combination fitting of the Cr-Bauxsol™ EXAFS data gave identical results with an R-factor of 4.2 % (data not shown).

The similarity in the chemistry of Cr(III) associated with hematite, sodalite and Bauxsol™ was also evident from shell fitting of the EXAFS data (Table 2). The coordination number and bond distance of both 1st shell O atoms and 2nd shell Cr atoms are similar to those reported for Cr(III) sorbed to γ-Al_2O_3 (at pH 4.3) [19], silica [20] and single crystals of hematite [21], but also γ-CrOOH [19, 20]. In fact, the fits obtained with the three materials are indistinguishable from γ -CrOOH [19, 20]. Therefore, the ability of Bauxsol™ to immobilise Cr(III) is a function of hematite and sodalite promoting Cr(III) polymerization and/or surface precipitation of γ-CrOOH.

3.4 Mn uptake

As for Cr(III), substantial Mn(II) uptake was only observed for the Bauxsol™ and hematite and sodalite reference minerals. In contrast to Cr(III), the Mn K-edge XANES spectra of Mn associated with the reference minerals were somewhat dissimilar to Mn-Bauxsol™ (Fig. 1e). In all cases the edge energy of Mn moved to a slightly higher energy (<2 eV) to that of aqueous $Mn(H_2O)_6^{2+}$ (Fig. 1e), suggesting partial oxidation of Mn(II) had occurred in the Bauxsol™ and reference minerals. In fact, the three spectra are extremely similar to that obtained during the bacterial oxidation of Mn(II) [22], where the XANES data were modelled successfully with the presence of three oxidation states (Mn(II), Mn(III) and Mn(IV)). Here, however, both the XANES (data not shown) and 1st derivative (Fig. 1j) Mn spectra were best reproduced when using Mn(II) (as an organic complex with malate rather than uncomplexed Mn; oxalate is present in some MBRRs) and the Mn(III)/Mn(IV) oxide birnessite, which has a reported oxidation state around 3.7 [23]. It is, therefore, clear that oxidation of Mn(II) has occurred and is likely to be a mechanism through which Mn is effectively retained by Bauxsol™. However, because of the presence of multiple Mn oxidation states, and therefore multiple coordination environments, modelling Mn beyond the 1st shell, is extremely difficult hence no structural parameters beyond the 1st shell O atoms are provided for Mn (Table 2).

3.5 U and Th uptake

There was strong uptake of Th, consistent with other studies [24], and U^{VI} [25-27]. The evolution of the aqueous Th concentrations (Fig. 2a) shows that there is a near complete removal of thorium from solution at all pH values, with >97% solids retention, even at pH 3, however a re-adsorption occurs during re-statting the pH at 3 overnight (Fig. 2a). Rojo et al. [24] suggest that almost complete binding of Th to ferrihydrite occurs at pH > 3.5 and magnetite at pH > 3.0 [24] through corner-sharing bidentate-mononuclear surface complexes, $(=FeO)_2Th^{2+}$. Similar binding sites exist on hematite. ICP-MS data for the additional elements analysed (Fig. 2b) show steady increases in Ca, Mg and Na (masked by the log scale) concentrations. Ca and Mg increases represent the destruction of the acid neutralising capacity (ANC) of the MBRR provided by the hydrotalcite and the para-aluminohydrocalcite (Table 1), and Na increases represent replacement from exchange sites by H^+, or erosion of sodalite, and cancrinite structures (Table 1). In addition, Al becomes increasingly soluble (Fig. 2b) and is indicative of the solubilisation of alumina, which is accompanied by a sharp decrease in U binding and K_d values (Fig. 2d). This suggests that a significant proportion of the bound U is associated with Al-(hydr) oxides (Table 1). Analyses for Fe and Ti show that both elements follow similar trends with an increase in concentration, by about an order of magnitude in samples at pH 4, but there is a slight re-precipitation at pH 3. An overnight re-equilibration at pH 3 (Fig 2b) a reduction in Na, Al, Fe, and Ti concentrations is also seen, which is commensurate with a re-adsorption of Th to the solids, suggesting that this re-adsorption may well be a co-precipitation with these elements.

Data for U^{VI} (Fig. 2c), and K_d values for ^{238}U loadings (Fig. 2d) show an adsorption maximum between pH 5 and 6; K_d values are >5000 mL/g (Fig. 2d). Either side of this adsorption maximum, U^{VI} binding to the MBRR surfaces declines with both increasing pH above pH 7 (K_d's <300 mL/g), and at pH below pH 5 (K_d's <100 mL/g). Uranium is usually present in oxidising waters as the cationic uranyl species (UO_2^{2+}), however this species is usually in complex forms

as uranyl-hydroxy and uranyl-carbonate complexes, except at low pH (e.g. [25-27]). The neutral, and negatively charged uranyl-carbonate complexes are not strongly sorbed [27], hence, systems at high pH have weaker U^{VI} retention (Fig. 2c & d). Greater ^{232}U is in solution than ^{238}U (Fig. 2d) because ^{238}U from the initial loading is irreversibly bound to the solids. In contrast to thorium, further U^{VI} is released from the solids during the overnight equilibration at pH 3.0 (Fig. 4), suggesting that there is continued mineral dissolution and associated release of U^{VI}. In addition, in systems containing U and Th in equal concentrations, they appear to compete for similar adsorption sites because a greater proportion of Th was released in the mixed 0.2 mM solution of U/Th than for the 0.2 mM Th solution alone (Fig. 3). Similarly Th apparently competes for U binding sites, as K_d values are also slightly lower for ^{238}U in the mixed system (Fig. 4b).

The isotope exchange between ^{238}U and ^{232}U can be used to estimate the amount of accessible (labile) uranium in the MBRR materials (Fig. 2e) with a linear exchange between tracer and weakly-bound solid-phase U^{VI} being observed [25, 28]. Isotope exchange does not occur with uranium in strongly bound forms, and for this reason the dynamics of available uranium can be estimated from the experimental results. A linear relationship between ^{238}U and ^{232}U in solution means that a fixed proportion of the ^{238}U is adsorbed by the MBRR except there is dissolution of mineral phases containing U. Non-leachable forms of U(VI) differed only slightly between experiments, however the proportion of occluded ^{238}U is greater in the 0.4 mM loadings (≈17%) than in the 0.2 mM loadings (≈12%; Fig. 6), and in the mixed 0.2 mM U/Th loadings (≈10%; Fig. 6). Much of the iron oxide crystallites present in MBRRs are very fine grained with an average crystallite size of 122 Å [29], and, as such, the crystallites often have many crystal defects. Such crystal defects allow for diffusion of adsorbed surface species to trans-locate from the surface to the lattice defect site by intra-particulate diffusion [30, 31], and remove some of the uranium from the accessible sites. Nagasaki et al. [32] found that intra particulate diffusion in poorly crystalline iron oxides occurs readily for the neptunium oxy-cations NpO_2^+, and diffusion is quite rapid at 2.0×10^{13} cm^2 s^{-1}; uranium diffusion behaviour is analogous. Aging of the material for 6 months (Fig 2f) shows that increased temperature, at increased loadings increased the amount occluded. These findings are consistent with previous diffusion studies, which show that solution concentration generates a diffusion gradient (higher concentrations re-distribute faster), and that the temperature, and diffusion time also control the re-distribution because of thermodynamic and rate limitations [30, 31, 33, 34]; these data also support the observations of Clark et al. [29].

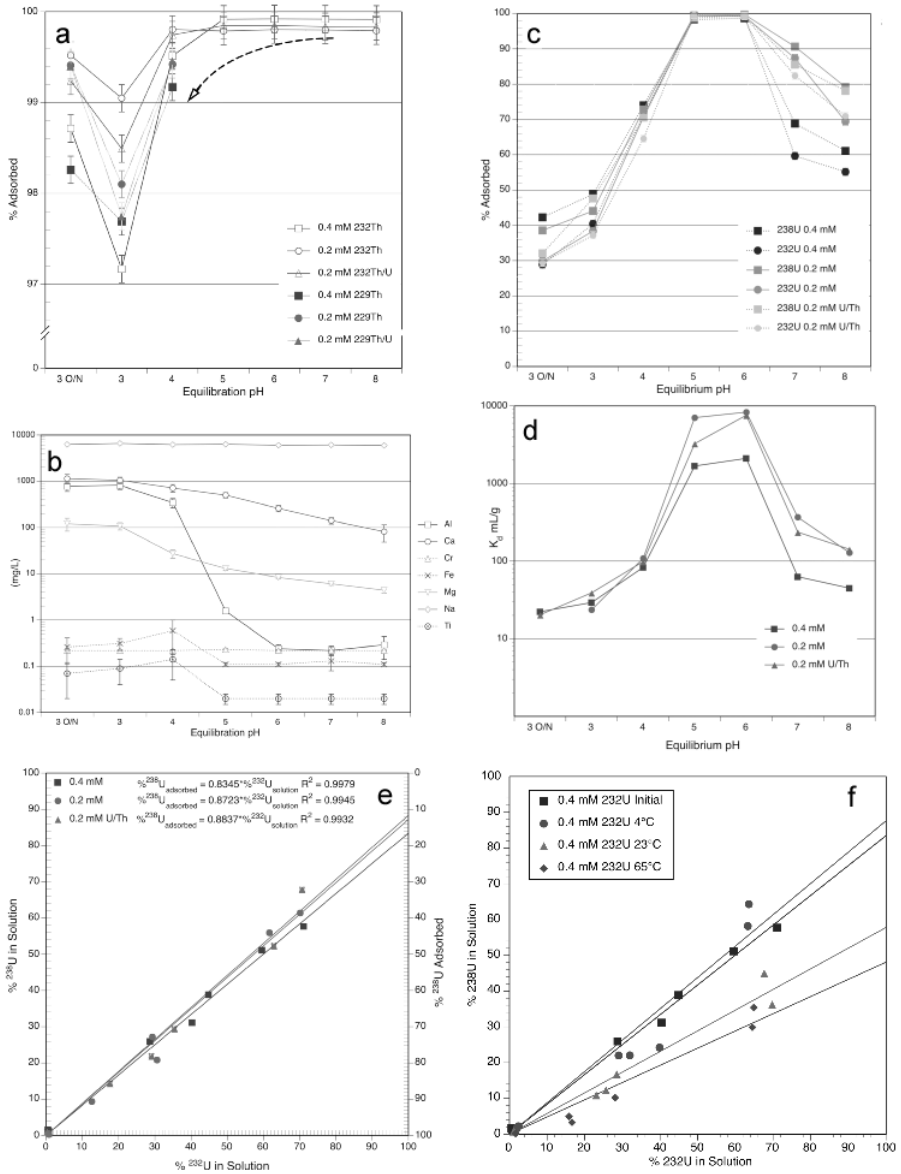

Figure 2. U and Th adsorption data; a) Thorium soption, b) Trace-metal concentrations, c) adsorption % for U isotopes, d) Kd values for the ^{238}U sorption data, e) Isotopic plot for initial loadings, f) isotopic plot for 0.4 mM loadings aged for 6 months at different temperatures

Although thorium isotope exchange data were also collected for all experiments, the low amount of thorium in solution means that the counting statistics prevented a similar analysis of reversibility of Th sorption from the solid. However, given the extremely strong association of thorium with the solid, it can be readily inferred that the amount of thorium released under most environmental conditions is likely to be very small. This work does raise the question of how rapidly, and how much U^{VI} is capable of being incorporated by intra-particulate diffusion. Consequently a follow-up study examining the incorporation of U^{VI} and Th in MBRR following extended aging (including elevated temperature) is currently being undertaken where isotope techniques will be applied to determine whether the amount of incorporation of U in MBRR increases during extended aging.

4. Conclusions

Trace-metal binding to MBRR's is a complex mix of processes, accentuated by the fine-grained nature of MBRR's and suite of mineral species capable of promoting adsorption. The adsorption of each metal to MBRR is controlled by different minerals in the system, where Cu uptake was controlled by hematite, Cr(III) by hematite and sodalite, Zn and Co immobilised by reaction with sodalite and/or gibbsite surfaces, and Mn(II) observed in association with hematite and sodalite. Synchrotron data modelling also indicate the means by which individual minerals contribute to metal immobilisation mechanisms. In addition, the isotopic exchange data for U and Th showed that once sorbed, occlusion begins primarily through intra-particle diffusion, and accelerates because of loading concentrations and with elevated temperatures over time.

5. Acknowledgements

We would like to thank AINSE for AINGRA08087, for the U and Th isotopic exchange work, and for Australian Synchrotron Grant 1648 2009/3 for the beam time at the Photon Factory, Japan.

References

1. Power, G.; Gräfe, M.; Klauber, C., Bauxite residue issues: I. Current management, disposal and storage practices. *Hydrometallurgy* **2011,** *108*, (1-2), 33-45.
2. Cooling, D. J.; Jamieson, E. In *Bauxite residues - A high volume resource*, Australasian Institute of Mining and Metallurgy Publication Series, Fremantle, 2004; Fremantle, 2004; pp 225-228.
3. Hanahan, C.; McConchie, D.; Pohl, J.; Creelman, R.; Clark, M.; Stocksiek, C., Chemistry of Seawater Neutralization of Bauxite Refinery Residues (Red Mud). *Environmental Engineering Science* **2004,** *21*, (2), 125-138.
4. Palmer, S. J.; Smith, M. K.; Frost, R. L., The effect of high concentrations of calcium hydroxide in neutralised synthetic supernatant liquor-Implications for alumina refinery residues. *Journal of Industrial and Engineering Chemistry* **In Press,** *10.1016/j.jiec.2010.10.009*.
5. Palmer, S. J.; Frost, R. L.; Smith, M. K., Minimising reversion, using seawater and magnesium chloride, caused by the dissolution of tricalcium aluminate hexahydrate. *Journal of Colloid and Interface Science* **In Press,** *10.1016/j.jcis.2010.09.062*.
6. McConchie, D.; Clark, M. W.; Hanahan, C.; Fawkes, R. In *The use of seawater-neutralised bauxite refinery residues (red mud) in environmental remmediation programs*, REWAS '99 Proceedings of the Global Syposium on recycling, waste treatment and clean technology, San Sebastian, Spain, 1999; Goballah, I.; Hager, J.; Solozabal, R., Eds. San Sebastian, Spain, 1999; pp 391-400.
7. Schwertmann, U.; Fechter, H.; Taylor, R. M.; Stanjek, H. In *A lecture and demonstration for students on iron oxide formetion*, Clays Controlling the Environment, Adelaide, July 18 to 23, 1993, 1995; Churchman, G. J.; Fitzpatrick, R. W.; Eggleton, R. A., Eds. CSIRO, Melbourne: Adelaide, July 18 to 23, 1993, 1995; pp 11-14.
8. Deer, W. A.; Howie, R. A.; Zussman, J., *An Introduction to the Rock Forming Minerals*. 15 th ed.; Longman: Hong Kong, 1985.9. ASRP *Average v. 2.0 for Windows*, Synchrotron Research Program: Sydney, Australia, 2007.
10. Ravel, B.; Newville, M., ATHENA, ARTEMIS, HEPHAESTUS; data analysis for X-ray absorption spectroscopy using IFEFFIT. *Journal of Synchrotron Radiation* **2005,** *12*, 537-541.
11. Downward, L.; Booth, C. H.; Lukens, W. W.; Bridges, F. In *A variation of the F-test for determining statistical relevance of particular parameters in EXAFS fits. X-ray Absorbance Fine Structure*, XAFS13: 13th International Conference - 2007, 2007; 2007; pp 129-131.
12. Harrison, J. J.; Zawadzki, A. W.; Chisari, R.; Wong, H., Rapid determination of uranium, thorium, plutonium, americium and strontium activities in water, soil and vegetation. *Journal of Environmental Radioactivity* **In Press,** *DOI: 10.1016/j.jenvrad.2010.05.010*.
13. Peacock, C. L.; Sherman, D. M., Copper(II) sorption onto goethite, hematite and lepidocrocite: a surface complexation model based on ab initio molecular geometries and EXAFS spectroscopy. *Geochim. Cosmochim. Acta* **2005,** *68*, (12), 2623-2637.
14. Cheah, S. G., .; Brown Jr., G. E.; Parks, G. A., XAFS study of Cu model compounds and Cu2+ sorption products on amorphous SiO2, g-Al2O3, and anatase. . *American Mineralogist* **2000,** *85*, 118-132.
15. Trainor, T. P.; Brown Jr., G. E.; Parks, G. A., Adsorption and precipitation of aqueous Zn(II) on alumina powders. *Journal of Colloid and Interface Science* **2000,** *231*, 359-372.
16. Roberts, D. R.; Ford, R. G.; Sparks, D. L., Kinetics and mechanisms of Zn complexation on metal oxides using EXAFS spectroscopy. *Journal of Colloid and Interface Science* **2003,** *263*, 364-376.
17. Ha, J.; Trainor, T. P.; Farges, F.; Brown Jr., G. E., Interaction of aqueous Zn(II) with hematite nanoparticles and microparticles. Part 1. EXAFS study of Zn(II) adsorption and precipitation. *Langmuir* **2009,** *25*, (10), 5574-5585.
18. d'Espinose de la Caillerie, J. B.; Kermarec, M.; Clause, O., Impregnation of g-alumina with Ni(II) or Co(II) ions at neutral pH: hydrotalcite-type coprecipitate formation and characterization. *Journal of the American Chemical Society* **1995,** *117*, 11471-11481.
19. Fitts, J. P.; Brown Jr., G. E.; Parks, G. A., Structural evolution of Cr(III) polymeric species at the g-Al2O3/water interface. *Environ. Sci. Technol.* **2000,** *34*, 5122-5128.
20. Fendorf, S. E.; Lamble, G. M.; Stapleton, M. G.; Kelley, M. J.; Sparks, D. L., Mechanisms of chromium(III) sorption on silica. 1. Cr(III) surface structure derived by extended X-ray absorption fine structure spectroscopy. *Environ. Sci. Technol.* **1994,** *28*, 248-289.
21. Grolimund, D.; Trainor, T. P.; Fitts, J. P.; Kendelewicz, T.; Liu, P.; Chambers, S. A.; Brown Jr., G. E., Identification of Cr species at the aqueous solution-hematite interface after Cr(VI)-Cr(III) reduction using GI-XAFS and Cr L-edge NEXAFS. *Journal of Synchrotron Radiation* **1999,** *6*, 612-614.
22. Webb, S. M.; Dick, G. J.; Bargar, J. R.; Tebo, B. M., Evidence for the presence of Mn(III) intermediates in the bacterial oxidation of Mn(II). *Proceedings of the National Academy of Science* **2005,** *102*, (15), 5558-5563.
23. McKeown, D. A.; Post, J. E., Characterization of manganese oxide mineralogy in rock varnish and dendrites using X-ray absorption spectrocopy. *American Mineralogist* **2001,** *86*, 701-713.
24. Rojo, I.; Seco, F.; Rovira, M.; Giménez, J.; Cervantes, G.; V., M.; de Pablo, J., Thorium sorption onto magnetite and ferrihydrite in acidic conditions. *J. Nucl. Mats.* **2009,** *385*, 474-478.

25. Payne, T. E.; Hatje, V.; Itakura, T.; McOrist, G. D.; Russell, R., Radionuclide applications in laboratory studies of environmental surface reactions. *Journal of Environmental Radioactivity* **2004,** *76*, (237-251).
26. Waite, T. D.; Davis, J. A.; Fenton, B. R.; Payne, T. E., Approaches to modelling uranium(VI) adsorption on natural mineral assemblages. *Radiochim. Acta* **2000,** *88*, 687-693.
27. Davis, J. A.; Meece, D. E.; Kohler, M.; Curtis, G. P., Approaches to surface complexation modeling of uranium(VI) adsorption on aquifer sediments. *Geochim. Cosmochim. Acta* **2004,** *68*, 3621–3641.
28. Del Nero, M.; Salah, S.; Miura, T.; Clement, A.; Gauthier-Lafaye, F., Sorption / desorption processes of uranium in clayey samples from the Bangombe Reactor Zone, Gabon. *Radiochim. Acta* **1999,** *87*, 135-149.
29. Clark, M.; Berry, J.; McConchie, D., The long-term stability of a metal-laden Bauxsol™ reagent under different geochemical conditions. *Geochem: Explor: Environ: Anal* **2009,** *9*, 101-112.
30. Axe, L.; Anderson, R., Experimental and theoretical diffusivities of Cd and Sr in hydrous ferric oxide. *Journal of Colloid and Interface Science* **1997,** *185*, 436-448.
31. Axe, L.; Anderson, R., Intraparticle diffusion of metal contaminants in amorphous oxide minerals. In *Adsorption of Metals by Geomedia, Variables, Mechanisms, and Model Applications*, Jenne, E. A., Ed. Academic Press: San Diego, 1998; pp 193-208.
32. Nagasaki, S.; Tanaka, S.; Todoriki, M.; Suzuki, A., Surface sorption and surface diffusion of NpO_2+with poorly crystallized ferric oxide. *Journal of Alloys and Compounds* **1998,** *271-273*, 252-256.
33. Buekers, J.; Amery, F.; Maes, A.; Smolders, E., Long-term reactions of Ni, Zn and Cd with iron oxyhydroxides depend on crystallinity and structure and on metal concentrations. *European J. Soil Sci.* **2008,** *59*, (4), 706-715.
34. Axe, L.; Trivedi, P., Intraparticle surface diffusion of metal contaminants and their attenuation in microporous amorphous Al, Fe, and Mn oxides. *Journal of Colloid and Interface Science* **2002,** *247*, (2), 259-265.